NTNU – Trondheim
Norwegian University of
Science and Technology

Pressure Fluctuations in Steady State Two-Phase Flow in Porous Media

Daniel Lisø

Master of Science in Physics and Mathematics
Submission date: June 2013
Supervisor: Alex Hansen, IFY

Norwegian University of Science and Technology
Department of Physics

Pressure Fluctuations in Steady-State Two-Phase Flow in Porous Media

Daniel Lisø

Preface

All the work on this thesis has been done in collaboration with Sjur Peder Helland. I am very grateful to have had his cooperation.

I would like to thank our supervisor, Alex Hansen, both for the interesting assignment, and for his help along the way.

Another great help has been Santanu Sinha, who wrote the simulation software. He has also helped with problems that have appeared while working with the thesis.

Ken Tore Tallakstad has supplied us with information about flow experiments being performed at the University of Oslo, for which we are grateful.

Finally, I want to thank the rest of the flow group at NTNU – our weekly meetings have given valuable input and ideas.

Daniel Lisø

Contents

Abstract

Several aspects of two-phase flow in porous are examined numerically. The burst size distributions in both the invasion phase and steady state are computed; above a threshold, the steady state distribution is found to be distributed according to a power law with exponent $\alpha = 2 \pm 0.1$. Spatial correlation and autocorrelation is investigated.

1 Introduction

Flow in porous media is an interesting and important subject in fields ranging from oil recovery to medicine. From a physics standpoint, the complex structures observed in multiphase flow are especially interesting. Much work, both experimental and numerical, has been done on invasion systems, where one fluid is injected into a system filled with another fluid.

This thesis focuses on the flow behavior in the steady state regime, which sets in after the invasion is finished. The burst size distribution for the steady state is examined, as is the pressure correlation function.

2 Theory

2.1 Porous media

A porous medium is a solid material that isn't solid throughout, but contains within itself many connected pores. An important material property of a porous medium is its porosity or void fraction, which is defined as

$$\phi = \frac{V_{\text{void}}}{V_{\text{total}}}, \tag{1}$$

where V_{total} and V_{void} are respectively the total volume of the material and the volume of the pores in the material. There are many natural porous media, for instance sandstone and limestone. There are also man-made porous media – one of the most interesting examples being aerogels, which can achieve $\phi \approx 0.99$. [19]

Another important property of a porous medium is its permeability, k. Permeability is a measure of how easily a fluid can flow through the material when a pressure difference is applied. Its role is similar to that of conductance in electricity. It is defined as

$$k = v\,\frac{\mu\,\Delta x}{\Delta P}, \tag{2}$$

where v is the bulk flow rate through the medium, μ is the viscosity of the fluid, Δx is the length of the medium, and ΔP the pressure difference across it.

2.2 Flow and fluid parameters

2.2.1 Capillary number

The flow through a porous medium is characterized by a few parameters. One of these is the capillary number, which describes the ratio between capillary and viscous forces, and is defined as

$$Ca = \frac{\mu_{\text{eff}} Q_{\text{total}}}{\gamma A}, \tag{3}$$

where μ_{eff} is the effective viscosity, Q_{total} is the total flow through the system, γ is the surface tension between the two fluids, and A is the total cross section of the inlets.

When $Ca \approx 1$, a relatively large value, viscous forces are dominant. For $Ca \ll 1$, capillary forces dominate. This ratio determines both quantitative and qualitative properties of the flow. Its effect is most dramatic during the invasion phase, but some steady state phenomena, such as the cluster size distribution, also depend on it. [22]

2.2.2 Viscosity ratio

Viscosity is a measure of a fluid's resistance to deformation when stress is applied. In two-phase flow, the ratio of the two fluids' viscosity is important for the behavior of the flow. We assume that one of the fluids is perfectly wetting, while the other is perfectly non-wetting, and define the viscosity ratio as

$$M = \frac{\mu_{\text{nw}}}{\mu_{\text{w}}}, \tag{4}$$

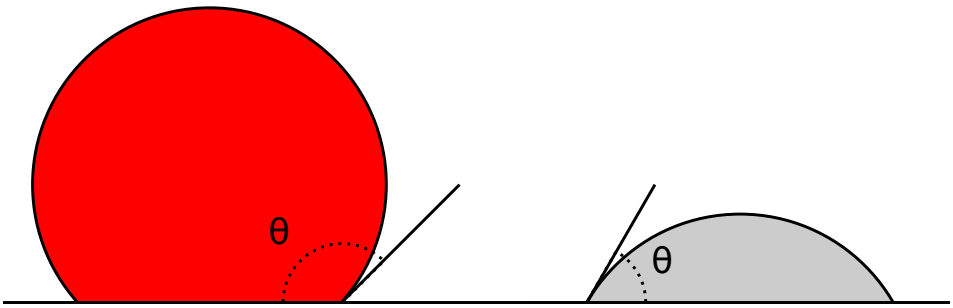

Figure 1: Wetting (grey) and non-wetting (red) fluid droplets on a surface. θ is the wetting angle.

where μ_{nw} is the viscosity of the non-wetting fluid and μ_{w} is the viscosity of the wetting one. This ratio can be a difficult value to control in experimental studies, since viscosities can be very temperature dependent. [6]

2.2.3 Wettability

When a fluid is placed on a smooth surface, it will spread out across the surface because of adhesive forces between the surface and the fluid itself. Opposing this are cohesive forces within the fluid. A drop of fluid on a surface will resemble a truncated sphere. Figure 1 illustrates this. The balance between these forces determines the contact angle θ the fluid makes with the surface.

Fluids can be categorized according to their wetting angle:

$$\text{Wetting}: 0^\circ \leq \theta \leq 90^\circ \tag{5a}$$

$$\text{Non-wetting}: 90^\circ \leq \theta \leq 180^\circ \tag{5b}$$

The special cases $\theta = 0^\circ$ and $\theta = 180^\circ$ are called respectively perfect non-wetting and perfect wetting.

2.2.4 Interface tension

The interface tension γ determines the pressure difference across an interface between two fluids.

2.3 Governing equations

2.3.1 Navier–Stokes equation

On the pore-level, two-phase flow in a porous medium is a two-phase interface flow of newtonian fluids. The fluids' motion is determined by the Navier–Stokes and continuity equations. The Navier–Stokes equation, when ignoring gravity and body forces, is

$$\rho \frac{\partial \mathbf{u}}{\partial t} + \rho \mathbf{u} \cdot \nabla \mathbf{u} = -\nabla p + \mu \nabla^2 \mathbf{u}, \tag{6}$$

and the continuity equation is

$$\nabla \cdot \mathbf{u} = 0 \tag{7}$$

The quantities involved are ρ, the fluid density; $\mathbf{u}$, the fluid velocity; p, pressure; and μ, the viscosity.

We also have the following boundary conditions:

- $\mathbf{u} = 0$ at the pore walls.
- Matching velocities on each side of the fluid interfaces.
- The pressure difference caused by the interface must be balanced by the forces in each fluid.

It is not feasible to solve these equations analytically.

2.3.2 Darcy's law

Darcy's law is an experimental relation, originally obtained by studying water flowing through a cylinder filled with sand. It has nonetheless been found to apply to many different systems. Ignoring body forces, the law is stated as

$$Q = \frac{AK}{\mu} \nabla p. \tag{8}$$

A is the cross sectional area of the material normal to the flow direction, K is the permeability, and ∇p the global pressure gradient. It describes the flow of a single fluid through a porous medium.

While originally a phenomenological relation, Darcy's law has since been derived from the Navier–Stokes equation. [11] That does not necessarily mean it applies to any flow, but it is assumed to be accurate for low flow rates. [20]

It is possible to extend Darcy's law to also describe multiphase flow by introducing effective fluid parameters:

$$Q_{\mathrm{w}} = -\frac{AK_{\mathrm{w}}^{\mathrm{eff}}}{\mu_{\mathrm{w}}}\nabla p \tag{9a}$$

$$Q_{\mathrm{nw}} = -\frac{AK_{\mathrm{nw}}^{\mathrm{eff}}}{\mu_{\mathrm{nw}}}\nabla p, \tag{9b}$$

where K_{eff} is an effective permeability that depends on capillary number, viscosity ratio and wettability, among other parameters.

2.3.3 Hagen–Poiseuille flow and the Washburn equation

By assuming steady, fully-developed and axi-symmetrical flow, with no radial or swirl components, the Navier–Stokes equation reduces to

$$\frac{1}{r}\frac{\partial}{\partial r}\left(r\frac{\partial u_x}{\partial r}\right) = \frac{1}{\mu}\frac{\partial p}{\partial x}. \tag{10}$$

If we further assume that the velocity is zero at the wall, we get

$$u_x = -\frac{1}{4\mu}\frac{\partial p}{\partial x}\left(R^2 - r^2\right), \tag{11}$$

and taking the average of this over the cross section of the tube leads to

$$\langle u_x \rangle = \frac{1}{2}\frac{R^2}{4\mu}\left(-\frac{\partial p}{\partial x}\right). \tag{12}$$

Assuming linear pressure drop down the tube, we end up with

$$\Delta P = \frac{8\mu LQ}{\pi r^4}, \tag{13}$$

which is known as the Hagen–Poiseuille equation. $\langle u_x \rangle$ has been multiplied by the cross sectional area to get Q, the total flow rate. L is the length of the tube.

Washburn [23] obtained the following equation from the Hagen–Poiseuille equation

$$\frac{\partial l}{\partial t} = \frac{\sum P}{8r^2 \mu l} \left(r^4 + 4\epsilon r^3 \right). \tag{14}$$

The sum runs over all participating pressures, and ϵ is called the coefficient of slip. Assuming that the wetting fluid perfectly wets the walls, in a horizontal flow network, this can be simplified to

$$Q = -\frac{\pi r^2 k}{\mu} \frac{\sum P}{l}. \tag{15}$$

$k = r^2/8$ is the permeability of a single tube, and is different from the permeability in Darcy's law.

2.3.4 Young-Laplace equation

The Young-Laplace equation is a relation describing the capillary pressure difference across the interface between two static fluids. With Δp denoting the pressure difference, $\hat{n}$ the unit normal vector out of the surface, and γ the surface tension, it reads

$$\Delta p = -\gamma \nabla \cdot \hat{n} \tag{16}$$

2.4 Drainage and imbibition

In a displacement process, where the material is initially filled with one fluid and another one is injected, the fluid being injected is called the invading fluid, while the one in the material is called the defending fluid. If the invading fluid is wetting and the defending fluid is non-wetting, the process is called imbibition. The inverse process, where the invading fluid is non-wetting and the defending fluid is wetting, is known as drainage.

The fluid movement at the pore level is different for these processes. In drainage, the invading fluid will get stuck at the constrictions in the pores. In imbibition, capillary suction will pull it through the constrictions, but it will

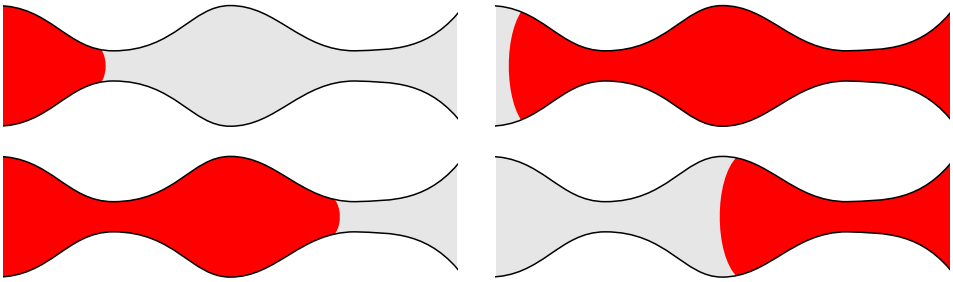

Figure 2: Drainage (left) and imbibition (right).

get stuck at the widest points of the pore. The pore level behavior is shown in figure 2. Lenormand et al. [12] gives a detailed study of the two processes.

2.4.1 Flow phases

Many studies, both experimental and numerical, have been done on the invasion of one fluid into a medium initially filled with another fluid. These have usually only considered the behavior up until the invading fluid reaches the outlet. We call this the invasion phase.

If one keeps injecting fluid into the system even after the invasion front has reached the outlet, the system eventually enters a steady state.

Transient phase – invasion

Much experimental and numerical work has already been done on the invasion phase, and the behavior is fairly well understood. Different flow patterns arise for various combinations of the capillary number and viscosity ratio, and they can be accurately described by different geometrical models. Outlines of these models are given in appendix B. Figure 3 shows which flow parameters lead to which flow pattern.

A small Ca leads to capillary fingering, for which invasion percolation is a good model. [5, 13, 24] Large Ca and small M gives stable displacement, which can be modelled as diffusion limited aggregation [14, 18]; large Ca and large M

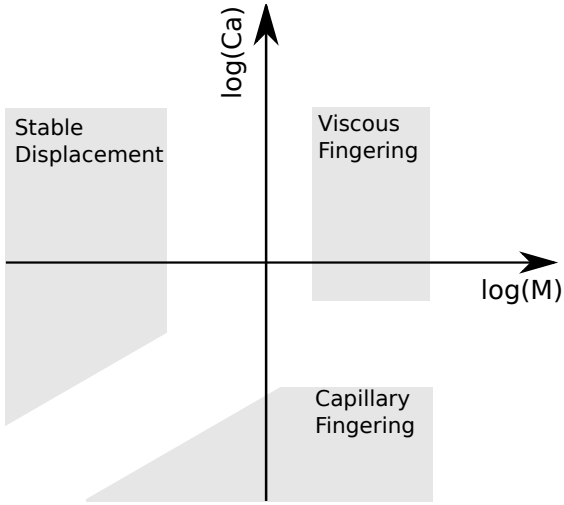

Figure 3: Flow regime phase diagram from Lenormand et al. [14]

gives viscous fingering, which can be modelled as anti-diffusion limited aggregation [4, 16, 18, 25]. Figure 4 shows how the different regimes look in experiments.

Steady state

For the steady state flow to be a state in the thermodynamic sense, there has to be a set of parameters that fully describe it, and it must be history-independent. Erpelding et al. [7] establishes that the statistical properties of the flow is independent of variations in the capillary number during the flow, which is evidence that steady state flow is a thermodynamic state.

2.4.2 Haines jumps

Haines [9] studied the behavior of water flowing through soil. He observed so-called pinning–jumping behavior, also known as Haines jumps, where the non-wetting fluid goes through a constriction into a larger portion of the pore, ac-

companied by a sudden drop in pressure. These events are also called bursts. When one happens, a relatively large area or volume can be invaded rapidly.

Figure 6 is an illustration of a porous medium just before and just after a burst. The defending, wetting fluid is shown in grey; the invading, non-wetting fluid in red. During the burst, the non-wetting fluid has invaded a relatively large are very quickly. The fluid involved in the burst moves an order of magnitude faster than the overall flow. [15]

During displacement, the burst size s is defined as the geometric area that is invaded during a burst. In steady state it is instead defined as the area a bubble sweeps during the burst.

2.5 Correlation

Correlation is a measure of dependence between quantities. For two random variables or datasets X and Y, the correlation coefficient is defined as

$$\rho_{X,Y} = \operatorname{corr}(X,Y) = \frac{\operatorname{cov}(X,Y)}{\sigma_X \sigma_Y} = \frac{E\left[\left(X-\mu_X\right)\left(Y-\mu_Y\right)\right]}{\sigma_X \sigma_Y}. \tag{17}$$

cov is the covariance operator, E is the expected value operator, μ_X and μ_Y are the expected values of variables X and Y, and σ_X and σ_Y are the standard deviations of variable X and Y.

The autocorrelation is the correlation of a signal with an offset copy of itself, i.e.

$$\operatorname{acorr}(X,n) = \operatorname{corr}(X_i, X_{i-n}). \tag{18}$$

The offset might for instance be in time, i.e. the correlation between a signal and itself delayed.

2.6 Power laws

A power law is a relation between two quantities f and x of the form

$$f(x) = ax^k, \tag{19}$$

where a and k are parameters.

One of the most interesting properties of power laws is that they are scale invariant. This means that $f(cx) \propto f(x)$:

$$f(cx) = a(cx)^k \tag{20a}$$

$$f(cx) = ac^k x^k \tag{20b}$$

$$f(cx) = ac^k f(x) \tag{20c}$$

A consequence of this scale invariance is that all power laws with the same exponent k are equivalent up to a scaling factor, which leads to another important property, called universality. Power laws with the same exponents show up in many very different systems. Such systems are said to belong to the same universality class.

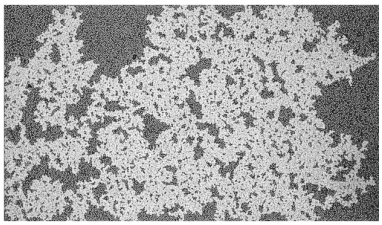

(a) Capillary fingering.

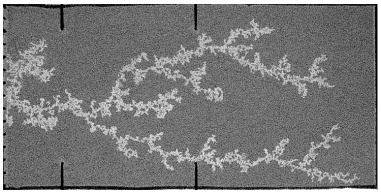

(b) Viscous fingering.

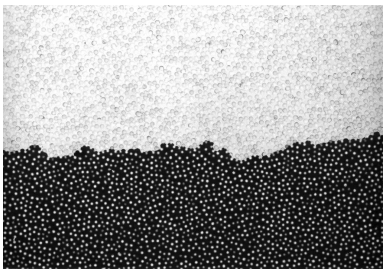

(c) Stable displacement.

Figure 4: Different invasion regimes. All figures from Tallakstad [21].

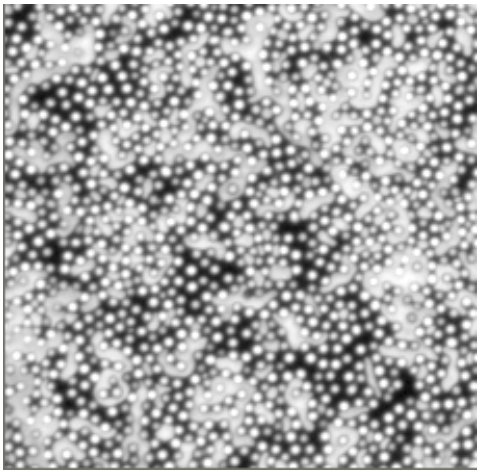

Figure 5: Close up of steady state flow experiment for $Ca \sim 10^{-2}$. [21]

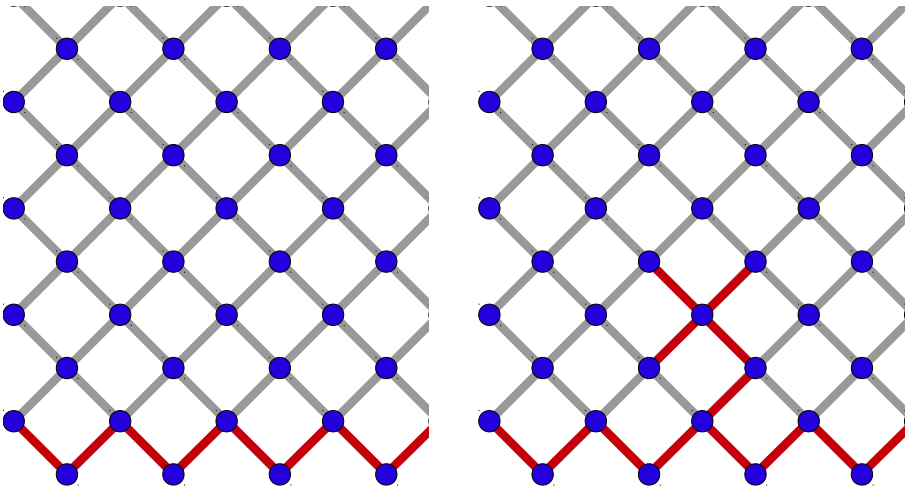

Figure 6: Network before and after a burst.

3 Method

3.1 Model

The model we use is based on the one described in Aker et al. [1, 2].

The medium is modelled as volumeless nodes connected by tubes, also called links. The tubes are approximated as cylinders when calculating flow rates, but as hourglass shaped when calculating capillary pressures. The nodes are placed on a rotated square grid, and are connected to their nearest neighbours; the geometry is illustrated in figure 6. Each node has a total of four neighbours. The system is periodic in its width. This necessarily means that all tubes are of the same length d. Real porous media are very irregular; to model this irregularity, the radii r_i of the tubes are chosen randomly such that $r_{\min} \leq r_i \leq r_{\max} \leq d$.

The model handles two different fluids, and assumes that one of them is perfectly wetting, while the other is perfectly non-wetting. The flow inside a single tube is modelled by the equations given in section 2, so the model as a whole inherits their assumptions, such as incompressibility. The fluids are also assumed to be immiscible; thus, where two fluids meet, they form a meniscus, and flow through the system as bubbles.

The bubbles are modelled as extending along the full width of the tube, so within a tube the flow is one-dimensional. Across the meniscus between two fluids, there is a pressure difference. With respect to the capillary pressure difference across a meniscus, the tubes are assumed to be hourglass shaped. Furthermore, the principal radius of curvature of the menisci is assumed equal to the radius at the point in the tube where the meniscus is located. Together with the Young–Laplace equation and wetting properties of the fluids – one perfectly wetting, one perfectly non-wetting – this gives the following expression for the pressure difference:

$$p_c = \frac{2\gamma}{r(x)} \left[1 - \cos\left(\frac{2\pi x}{d} \right) \right], \tag{21}$$

where γ and d are the surface tension and length of the tube, respectively, $r(x)$ is the radius of the tube, and x is the position within the tube. This relation makes it possible to account for small displacements of the interface within the

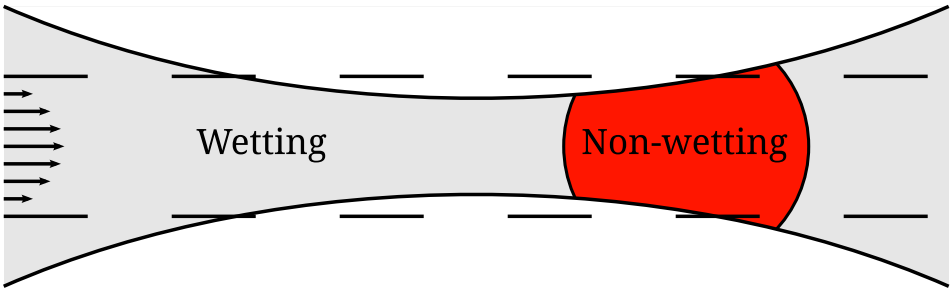

Figure 7: A single tube in the network, showing the different shapes that are assumed when calculating capillary pressure (solid lines) and flow (dashed lines).

tube, which are important for the burst dynamics. [8, 17] Figure 7 shows a single tube with a bubble, and illustrates the shape used to compute p_c.

The flow $q_{i,j}$ in a tube between nodes i and j is calculated with the Hagen–Poiseuille equation and Washburn's equation. The result is

$$q_{i,j} = \frac{-\sigma_{i,j} k_{i,j}}{\mu_{i,j}} \left(\frac{p_i - p_j - p^c_{i,j}}{d_{i,j}} \right), \tag{22}$$

where $\sigma_{i,j}$ and $k_{i,j}$ stand for the cross section and permeability of the tube connecting nodes i and j, and p_i and p_j are the pressures in nodes i and j. $\mu_{i,j}$ is the effective viscosity of all the fluid in the tube, defined as the average viscosity of the fluids weighted by how much there is of each, and $p^c_{i,j}$ is the sum of capillary pressures caused by the menisci in the tube.

The nodes are volumeless, so at any time, the amount of fluid flowing in must equal the amount flowing out:

$$\sum_j q_{i,j} = 0 \tag{23}$$

Combining equations 22 and 23 gives us the equation

$$\sum_j \frac{-\sigma_{i,j} k_{i,j}}{\mu_{i,j}} \left(\frac{p_j - p_i - p^c_{i,j}}{d_{i,j}} \right) = 0. \tag{24}$$

If we move the p^c to the right hand side, we can rewrite this as the matrix equation

$$D_{i,j} p_j = B_i, \tag{25}$$

where D is a conductivity matrix and B is a vector of capillary pressures. Given some boundary conditions, this is a solvable set of equations.

An iteration of the simulation roughly consists of moving the bubbles in the links according to equation 22, then, with the new positions of the bubbles, solving equation 25, and then starting over. As bubbles travel through nodes, new bubbles are created according to ad hoc but sensible rules; these are explained in more detail later.

The model in Aker et al. [1, 2] is periodic in both directions, and the flow is driven by applying a pressure between the top and bottom nodes when they wrap around. This necessitates solving the pressure field several times to keep the total flow Q constant, as it has to be. We want to examine the behavior when fluid is injected at the bottom and expelled at the top, with periodicity only along the width of the system. The fluids are to be injected in a certain pattern, alternating between wetting and non-wetting from left to right; see figure 12 for an example of the layout. The boundary conditions are therefore

- The bottom links of the bottom nodes are kept at a constant q.
- The top nodes are kept at at constant $p = 0$.

These changes are rolled into the B vector.

The bubbles are subject to the following rules:

- A limit is placed on how many bubbles of non-wetting fluid are allowed per tube. If there are more, the closest two are merged.
- The volume of each fluid flowing into a node is stored and used to create new bubbles in the tubes carrying fluids out of the node.
- If bubbles are closer than some threshold, they are merged.

3.2 Mixing length

Both wetting and non-wetting fluid is injected into the system. Because of this, close to the inlets, the two different fluids are mostly separated from each other. This is illustrated in figure 8. The distance between the inlet area and the first row where the fluids are properly mixed, is the mixing length l_{mix}.

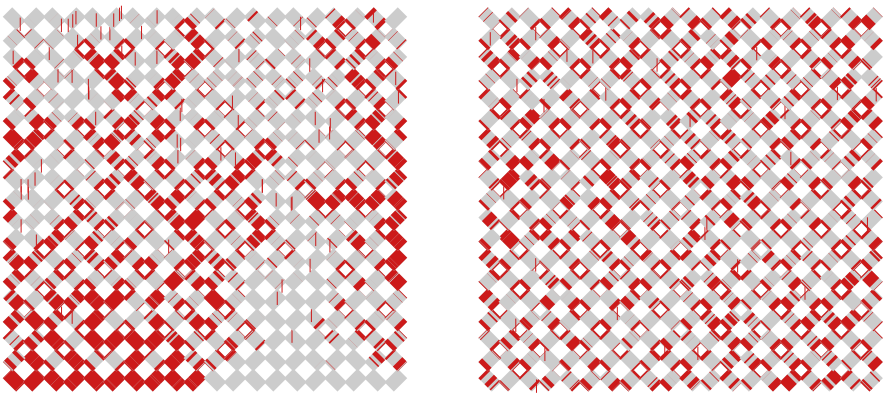

Figure 8: Bubble distribution close to (left) and further away from (right) the injection sites. Close to the injection sites, the fluids are not well mixed.

We want to do our measurements after the fluids are mixed. However, it is not clear how to determine l_{mix}, so to err on the side of caution, we set it at half the height of the system.

3.3 Finding the start of the steady state regime

Figure 9 shows the pressure signal for a selection of nodes throughout a system. The steady state starts when the pressure stabilizes, and as seen on the figure, this happens the same time for all nodes. For analysis purposes, we want to determine this automatically. Our algorithm for doing this is as follows:

- Compute the average pressure p' of the last 10 % of the pressure signal for each node.

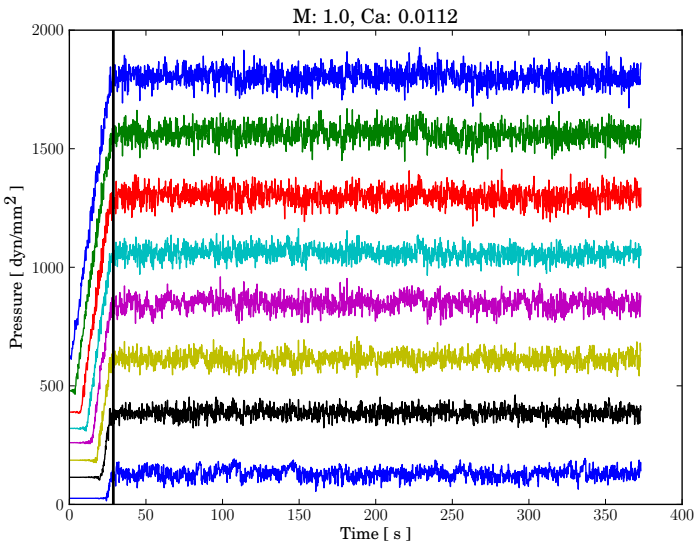

Figure 9: Pressure signal at various nodes. Steady state is reached when the pressure stabilizes, which happens simultaneously across the lattice.

- Find the time when at least 90 % of all nodes have reached their p'.

We use 90 % instead of 100 % to prevent outliers from destroying the results.

3.4 Defining a burst

Bursts were introduced in section 2.4.2. It is difficult to measure their geometrical size s. To get around this, we use the valley size

$$\chi = \sum_i \Delta p_i \tag{26}$$

where the Δp_i are the pressure *drops* within the burst, as a proxy, since it has been shown to be proportional to s.

A burst starts whenever the pressure drops, and lasts until it reaches the value it had when it started. We differentiate between inclusive and exclusive

Ca
$1.6 \cdot 10^{-3}$
$3.2 \cdot 10^{-3}$
$4.8 \cdot 10^{-3}$
$6.0 \cdot 10^{-3}$
$9.6 \cdot 10^{-3}$
$11.2 \cdot 10^{-3}$
$12.8 \cdot 10^{-3}$
$14.4 \cdot 10^{-3}$

Table 1: Capillary numbers.

burst; the former can start inside another burst, while the other can't. The two cases are illustrated in figure 11.

3.5 Finding the burst size distribution

The burst size distribution is constructed by making a histogram of the detected burst sizes χ. Because there are relatively few big bursts, and very many small ones, the histogram is constructed with logarithmic bin sizes.

3.6 Running the simulation

Simulations have been performed for all combinations of the capillary numbers in table 1 and $M = 0.1, 1, 10$, for a total of 24 simulations.

Other parameters were kept constant. All simulations were run with a system of 50 by 100 nodes, with 10 injection points for each fluid. 40 % of the injected fluid was non-wetting. All tubes were 1 mm long. The radii of the tubes were drawn randomly from a uniform distribution between 0.1 mm and 0.4 mm. A maximum of 3 bubbles were allowed per tube. The simulations were run for 200 000 time steps, and data was logged every 100 time steps. The system was initially completely filled with the wetting fluid.

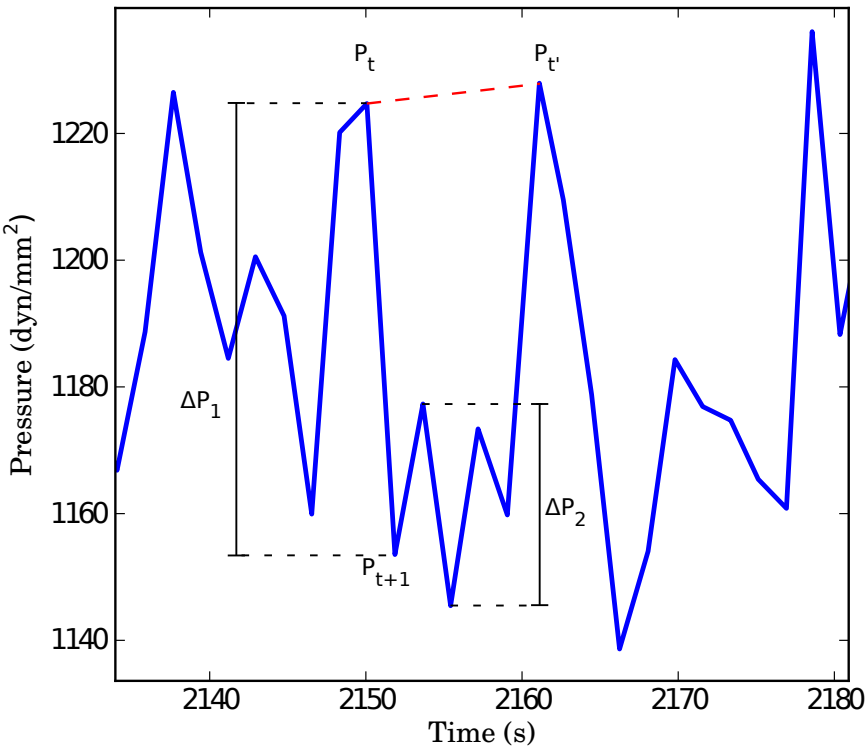

Figure 10: A burst in the pressure signal. It starts at t and lasts until t'.

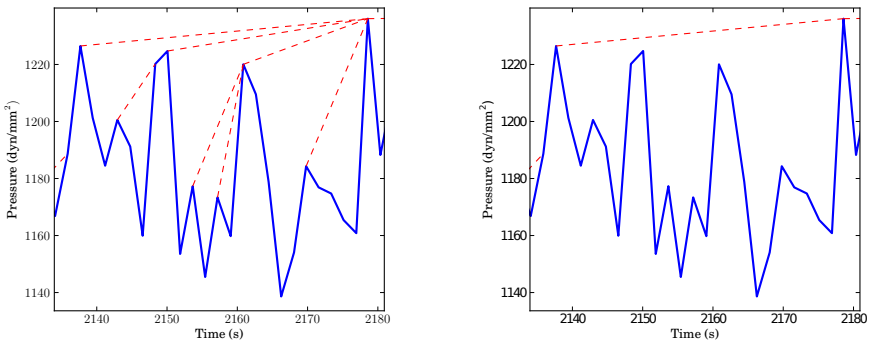

Figure 11: The difference between inclusive bursts (left), where bursts can start inside other bursts, and exclusive bursts (right), where they cannot.

Figure 12: The bottom of the system at the start of a simulation. The wetting fluid is grey, the non-wetting fluid is red.

4 Results and discussion

4.1 Burst size distributions

The burst size distributions have been computed for all M and Ca in both the transient and steady state regimes. Figures 13, 14 and 15 show the distributions in the steady state regime grouped by M; figure 16 shows all the steady state distributions at once. Each set of symbols corresponds to a capillary number.

Above some threshold, the datapoints fall along a straight line. A straight line in a log-log plot is indicative of a power law distribution with exponent α equal to the line's slope. There are many more small than large bursts, so to get useful statistics, the burst size histograms are made with logarithmic bins. Because of this, the slope of the line actually equals $\alpha + 1$. This is explained in more detail in appendix A.

To determine the power law exponent for a distribution, a straight line fit is performed on its tail. The results are summarized in table 2. As an uncertainty measure, we have used the sample standard deviation of the obtained slopes for the set of results used.

As seen in the figures and table 2, the exponent equals -2 with reasonable accuracy, regardless of viscosity ratio and capillary number. The figures show that the power law is valid across two orders of magnitude. This is the same exponent that has previously been determined for the exclusive distribution during drainage [3] and the exclusive distribution in steady state flow on a torus.

Figure 18 shows the distribution of exclusive bursts in the transient phase for all viscosity ratios and capillary numbers. Its shape is similar to that of the steady-state inclusive distributions, but only somewhat. The data is too spread

M	α
0.1	-1.971 ± 0.07
1.0	-2.005 ± 0.14
10.0	-2.124 ± 0.12
All	-2.034 ± 0.13

Table 2: Critical exponents α of the burst size distribution for each value of M.

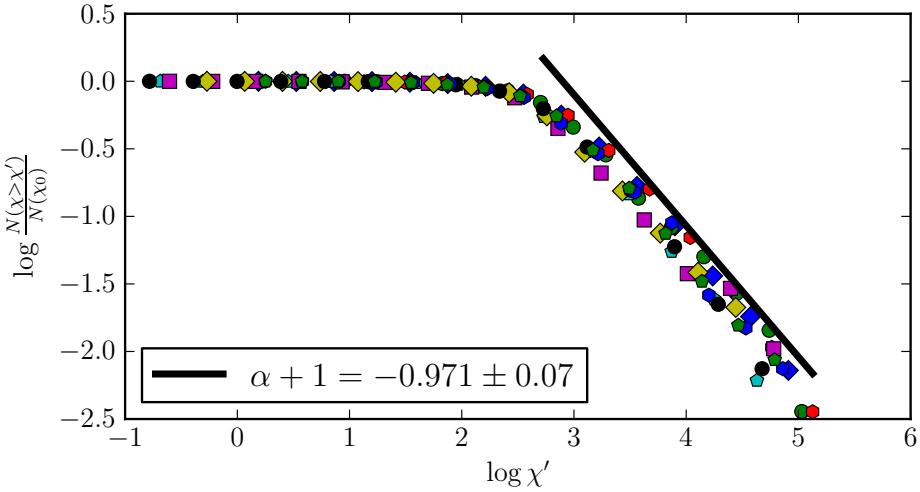

Figure 13: Steady state inclusive burst size distribution for $M = 0.1$ and all Ca, and straight line fit.

out for a good fit, and we end up with $\alpha = -2.324 \pm 0.69$.

There are some difficulties with gathering enough data for this case. For one thing, there are at best as many exclusive bursts as there are inclusive ones, and usually fewer. This isn't too big a problem here, though, as the pressure is increasing overall. Since we're looking at the transient phase, however, we are necessarily limited by its duration. The transient phase lasts until the injected fluid reaches the outlets, so its duration depends on the overall injection rate Q. Injection rate is determined via the capillary number – $Ca \propto Q$ – so we have also investigated the distribution for only the low Ca, but the results weren't much better; see figure 17.

The large uncertainty allows for α to be in the range ~1.63–3.01. It is therefore possible that $\alpha = 2$ for exclusive bursts in the transient regime. This would place it in the same universality class as steady-state flow on a torus, injection of one liquid into a system filled with another, and of course the steady-state regime in the current system.

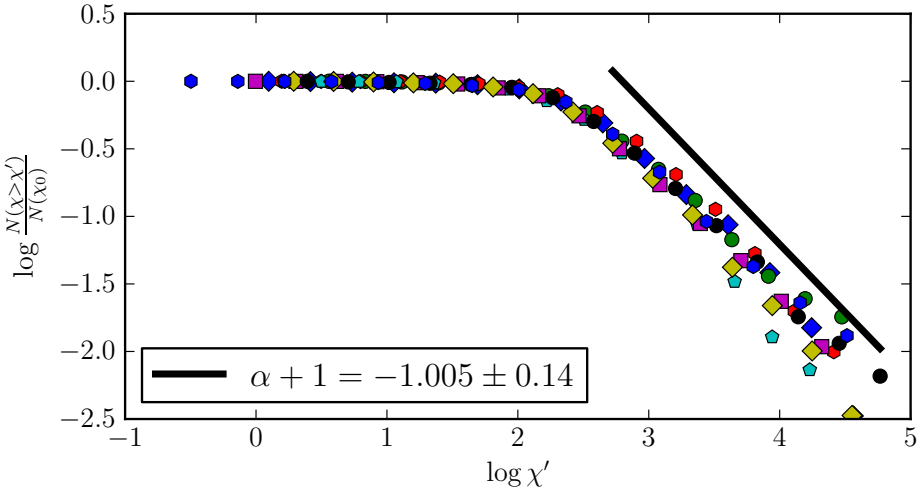

Figure 14: Steady state inclusive burst size distribution for $M = 1$ and all Ca, and straight line fit.

Hemmer and Hansen [10] investigated the failure size distribution in the fibre bunch model in a similar way to how we look at burst size distributions. Their results were that the exclusive distribution is a power law with exponent $\xi = 2.5$. Our result does not preclude $\alpha = 2.5$, so it possible that the exclusive burst dynamics in the transient are in the same class as exclusive fibre failures.

However, while our results don't preclude either of these possibilities, they don't clearly point to any of them either; the uncertainty is too large to draw any conclusions.

4.2 Pressure correlations

We have examined the correlation function ρ between nodes in the steady-state regime.

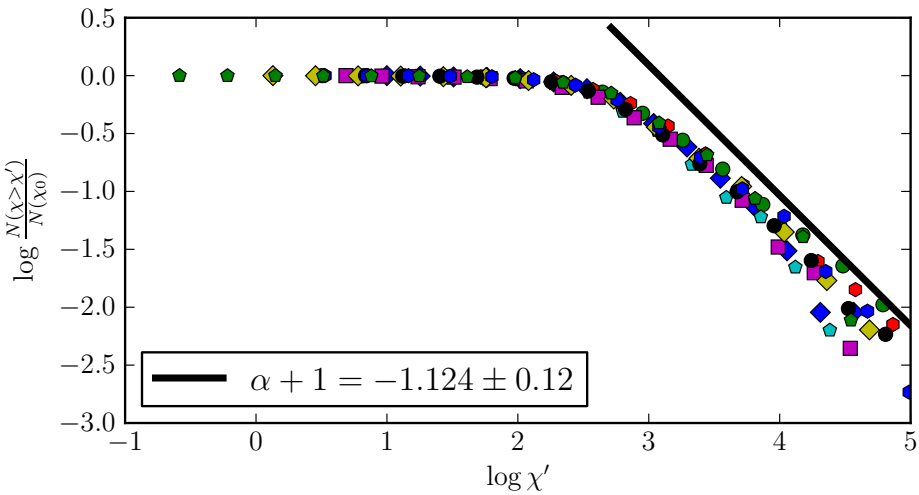

Figure 15: Steady state inclusive burst size distribution for $M = 10$ and all Ca, and straight line fit.

4.2.1 Spatial correlation function

Figure 22 shows typical spatial correlation plots. Figure 22a is the correlation between a single node and the rest of the nodes in the system. In figure 22b, each node is colored according to the mean of its correlation with the other nodes in the system; it's a plot of the quantity

$$\bar{\rho}_i = \frac{1}{N_{\text{nodes}}} \sum_j \rho_{i,j}, \tag{27}$$

where i and j represent nodes.

As seen in figure 22a, the correlation drops off with distance. Figure 23a illustrates this relationship in more detail. The plotted quantity is

$$\bar{\rho}\,(d) = \text{mean}\left(\left[\rho_{i,j} \text{ for all nodes where } |\Delta r_{i,j}| = d\right]\right). \tag{28}$$

The difference between figure 23a and 23b is that the first counts all node pairs

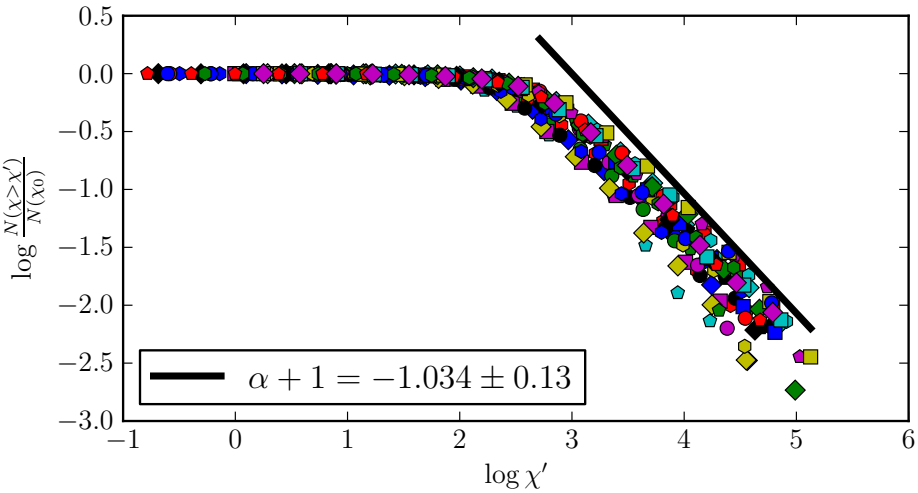

Figure 16: Steady state inclusive burst size distribution for all M and all Ca, and straight line fit.

where the nodes are d lattice units apart, while the second only counts pairs that are on either the same row or column.

For every combination of Ca and M, the average correlation as a function of distance between nodes nicely fits a curve of the form

$$f(r) = \frac{1}{(ar+1)^{1/2}}, \tag{29}$$

where a is a fitting parameter. The obtained fitting parameters are shown in figure 20. They seem to depend primarily on Ca, and not very much on M. It also looks like they plateau around $Ca = 0.010$.

The larger a is, the faster the correlation drops off as a function of distance. Since $Ca \propto Q$, this means that a faster overall flow gives a less coherent pressure development.

The system is 100 lattice units both wide and tall, but periodicity in the x-direction means that no nodes can be separated in the x-direction by more than 50 lattice units – thus the graph counting only same-row-pairs stops at 50.

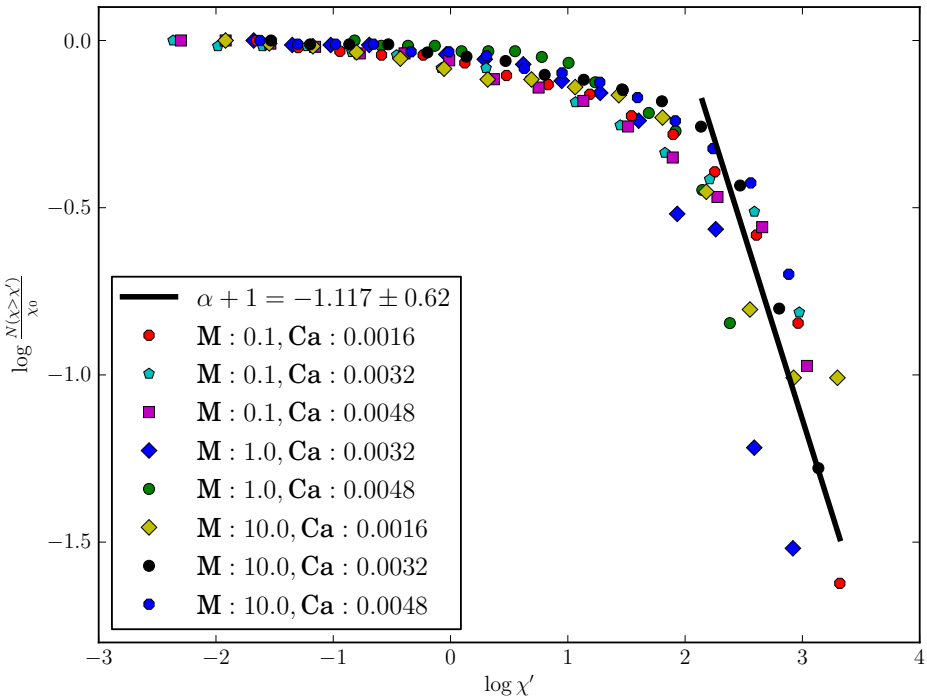

Figure 17: Exclusive burst size distribution in the transient phase for small values of *Ca*.

The graphs for same-row- and same-column-pairs never overlap perfectly, and eventually diverge significantly. This divergence is not unexpected, since one set of data is collected from node pairs laying along the overall flow direction, while the other is from pairs that lay across it.

Figure 24 shows the row averaged average correlation, i.e. the row average of the data shown in figure 22b. It peaks relatively close to the injection sites and subsequently drops to zero. The short climb at the start means that the nodes on the first few rows are more independent than the ones a little further away. This seems reasonable, since it's close to the injection points and the system has not had time to settle in.

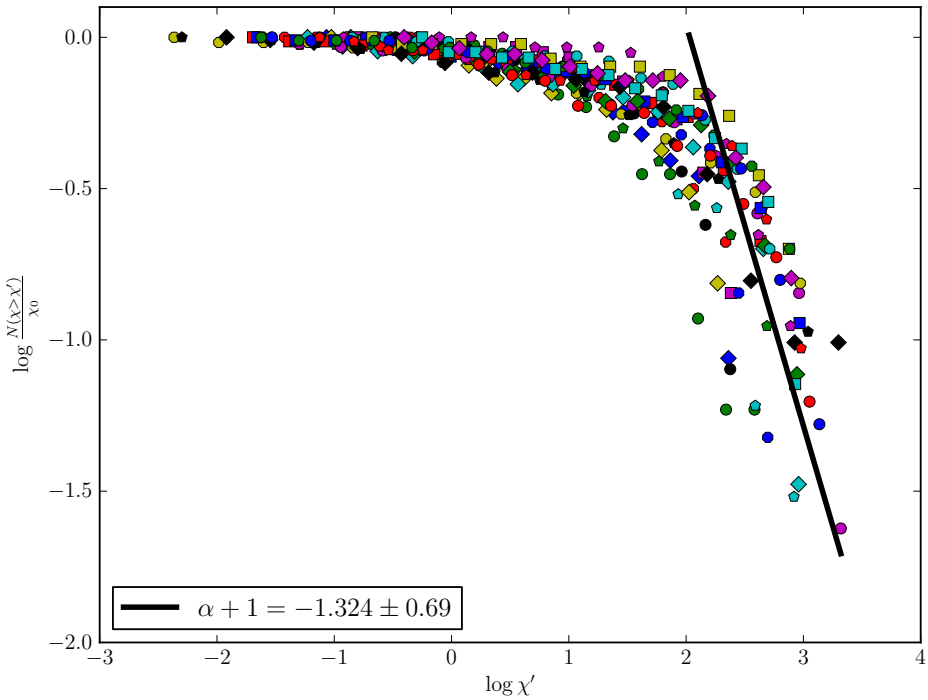

Figure 18: Exclusive burst size distribution in the transient phase for all values of M and Ca.

4.2.2 Autocorrelation

A typical autocorrelation plot of the pressure signal at a node is shown in figure 21. The autocorrelation at other nodes and for other M and Ca are similar.

The autocorrelation drops off linearly with the offset. This suggests an underlying autoregressive process, which is a process of the form

$$x_t = c + \sum_{j<t} \alpha_{t-j} x_{t-j} + \epsilon_t, \tag{30}$$

where the α are parameters and the ϵ are random numbers. The random walk is an example of an autoregressive model.

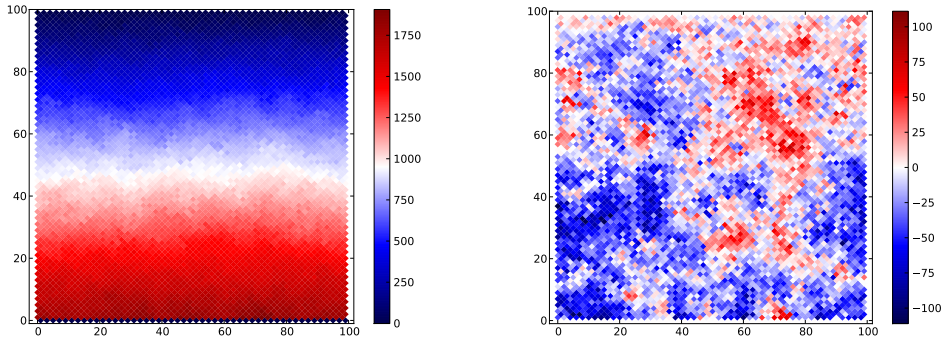

(a) Lattice pressure in steady state. Unit is dyn/mm^2.

(b) Lattice pressure in steady state minus linear component. Unit is dyn/mm^2.

Figure 19: Pressure in steady state flow.

The autocorrelation in pressure changes has also been examined. At one lag, it is significantly negatively correlated. For more than one lag, it is almost zero.

4.2.3 Correlations and system geometry

Figure 22b shows the average correlation between the pressure signal in a given node and every other node in the system. Figure 24 better illustrates the large-scale behaviour seen in figure 22b; it shows the average of each row against the distance from the injection sites. It's fairly stable at the bottom half of the system, then falls off as the outlet is approached.

There is also some finer structure visible at places; specifically, patches of lower average correlation than the neighbouring area. The relatively low correlation suggests that these patches are insulated from the rest of the system in some way. To examine this, we have saved the radii of the links in the system and made maps like figure 22b showing the minimum, mean and maximum radius of the links connected to a given node; see figures 25a, 25b and 25c. There are, however, not any obvious correspondence between the correlation map

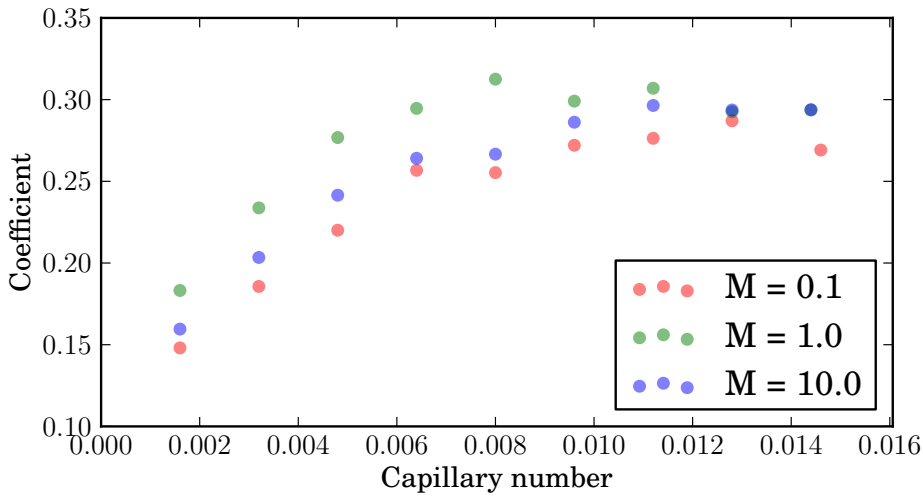

Figure 20: Parameter value of the correlation fit.

and radius maps.

4.3 Spatial pressure variation

Figure 19a shows a snapshot of the pressure in each node of the lattice for $M = 1$ and $Ca = 11.2 \cdot 10^{-3}$. Other values of M and Ca are similar. It appears to drop off approximately linearly with distance from the injection points, consistent with Darcy's law. Figure 19b shows the same data with the linear component subtracted.

Figure 26 show the row-averaged relative deviation from the Darcy pressure for different timesteps. It is fairly low up until the last 20 or so rows.

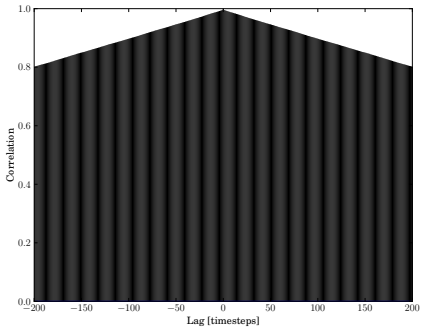

(a) Autocorrelation in pressure signal.

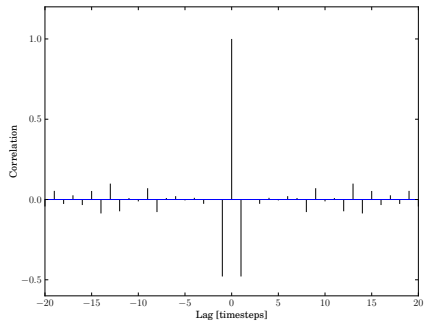

(b) Autocorrelation in pressure changes.

Figure 21: Autocorrelation plots.

4.4 Errors and inaccuracies

Model assumptions

The model has been compared with experimental results, and it reproduces much of the real behavior very well. Nonetheless, it is based on certain assumptions that potentially limit its applicability. For instance, it assumes that bubbles extend to the full width of the tubes. This assumption means that the model does not account for film flow, where one fluid flows past the other in a thin layer along the tube walls. Film flow effects have been observed at low capillary numbers by Tallakstad [21].

The model also assumes the fluids to be incompressible, and that one of them is perfectly wetting while the other is perfectly non-wetting. In many experiments, the defending fluid has been air, which is actually quite compressible. Lastly, the model does not account for viscosities varying with e.g. temperature.

Burst size

When computing the burst size distributions, we define the burst size χ as the sum of pressure drops (and only *drops* – the sum of all pressure changes would

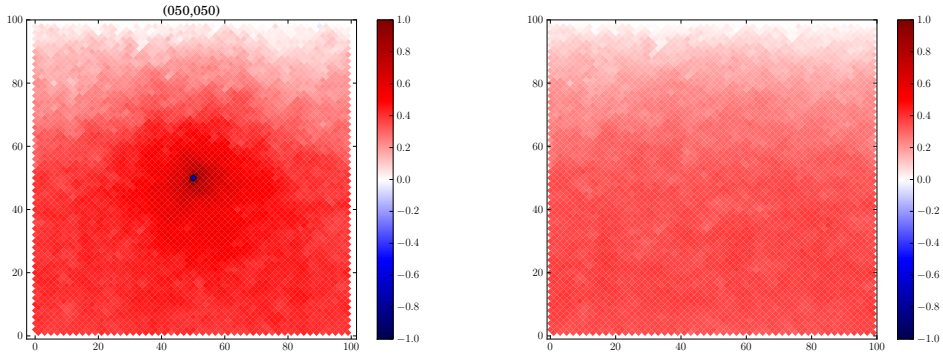

(a) Two-point correlation between the the point (50, 50) (in blue) and all other points.

(b) Average correlation between all points.

Figure 22: Correlation maps.

be rather uninteresting) within the burst. This quantity is used as a proxy for the thing we actually want to know about, which is the geometric burst size s. Furuberg et al. [8] established that $\chi \propto s$, albeit only for slow drainage in an invasion experiment. We have assumed the relation to be valid for our system as well, but we have not made efforts to verify this.

5 Conclusion

We have performed simulations of two-phase flow in a porous medium for a range of capillary numbers and viscosity ratios, and investigated some interesting quantities.

We have computed inclusive burst size distributions for the steady state, and exclusive distributions for the transient phase. The inclusive steady state distributions are found to be independent of both capillary number and viscosity ratio. This is shown in figures 13, 14, 15 and 16. Past some threshold value, the distributions are power laws. By fitting a straight line to this region, we determine the exponent α of the power law. When considering the distributions

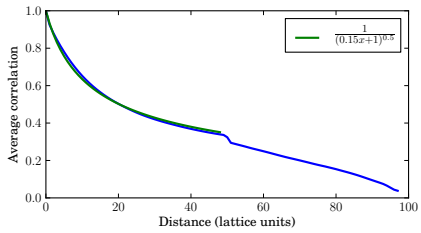

(a) Average correlation as a function of distance.

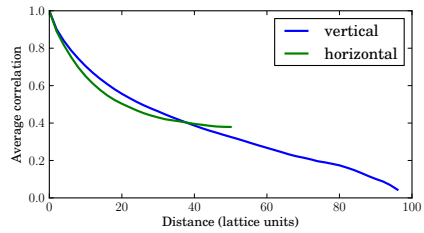

(b) Average correlation when only counting nodes that are on the same row or column.

Figure 23: Average correlation as function of distance for different counting schemes.

for all Ca and M, we find that $\alpha = 2.0 \pm 0.1$. As the figures show, this power law is valid for more than two orders of magnitude. This places our system in the same universality class as the steady state flow on a torus and invasion.

Exclusive burst size distributions in the transient phase were also computed. The distributions are roughly similar to the inclusive steady state ones. However, the limited duration of the transient phase, together with the fact that there are fewer exclusive than inclusive bursts, limits the amount of data we can gather in this phase. Trying to fit a power law to the data, we found that $\alpha = -2.324 \pm 0.69$. This is too large an uncertainty to draw any conclusions.

The large scale spatial pressure variations were found to be consistent with Darcy's law, except close to the system edges.

Various properties of the pressure signal correlation function ρ in steady state have been examined. The two-point correlation in pressure between nodes decreases as a function of the distance between the nodes. When looking only at nodes that are directly downstream from each other, the correlation eventually drops to zero. For nodes that are on the same row, the correlation drops off initially, then plateaus.

The average correlation as a function of node separation is qualitatively the same for all capillary numbers and viscosity ratios. How fast it drops off depends to some degree on the capillary number. To quantify this, we have performed curve fits on it with a one-parameter function, specifically $f(r) =$

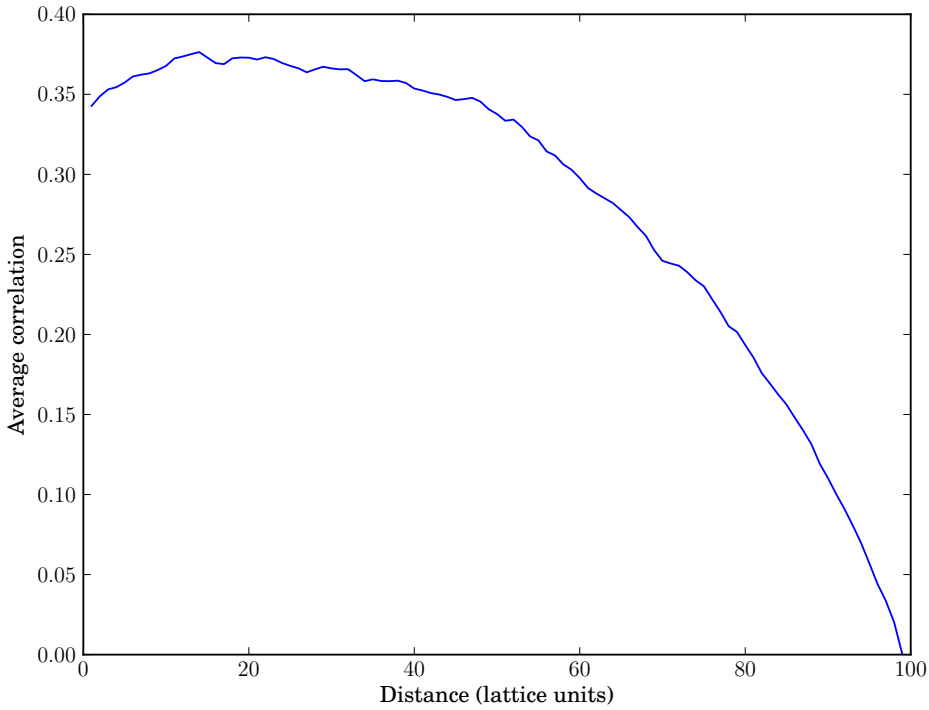

Figure 24: Row averaged average correlation coefficient as a function of distance from the inlet. The nodes closer to the inlet are more correlated to the system than the nodes far from the inlet

$1/(ar+1)^{0.5}$. This parameter, a, can then tell us the drop-off speed. It initially increases with Ca, then seems to plateau.

The autocorrelation of the pressure signal looks the same for all nodes in a system and all system parameters. It falls off linearly as the lag increases. This shape is typical of autoregressive processes.

The autocorrelation of pressure changes in steady state was also computed. At one lag, it is significantly negatively correlated. Since, in the steady state, the pressure generally fluctuates around a certain level, this is expected behavior. For more than one lag, however, the autocorrelation is very small.

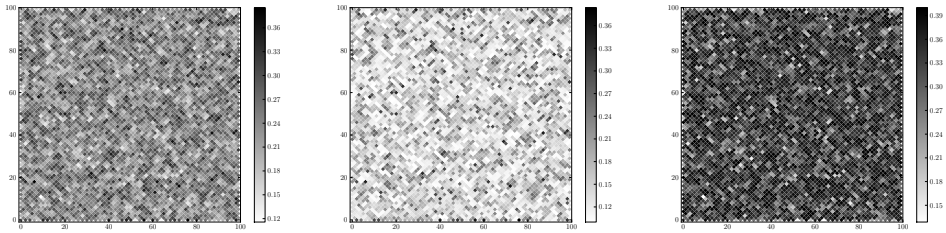

(a) Mean. **(b)** Minimum. **(c)** Maximum.

Figure 25: Mean, minimum and maximum radius of the tubes connected to each node.

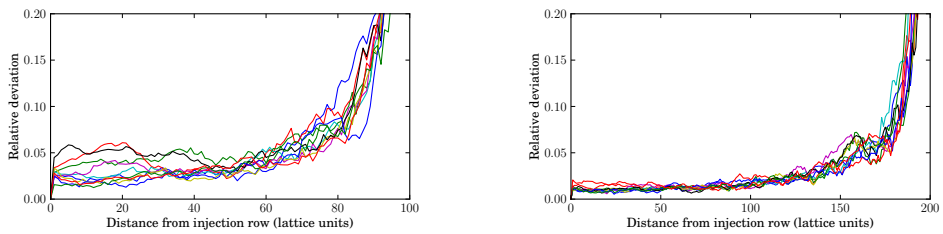

(a) Row-average relative deviation from Darcy Pressure on a 50 x 100 lattice.

(b) Row-average relative deviation from Darcy Pressure on a 50 x 200 lattice.

Figure 26: Relative deviation from Darcy pressure.

A Logarithmic binning

Given a random variable X with some probability density function $f_X(x)$ the probability that a sample of X lies on the interval $x < X < x + dx$ is defined as

$$\Pr(x < X < x + dx) = f_X(x)dx \tag{31}$$

If the probability density function is unknown it can be found by sampling the random variable multiple times and constructing a histogram of the results. The histogram consists of a set of bins, where each sample of the random variable is added to the bin corresponding to the value of the sample. It is evident

that the number of samples in each bin, n_i, is proportional to the probability density function of the random variable and the width of the bin, w_i.

$$n_i \propto w_i f_X(x) \tag{32}$$

If the PDF of the random variable is a exponential function, $f_X(x) \propto x^{-\alpha}$, the exponent α is found by regressing $\log(n)$ versus $\log(x)$

$$\log(n_i) \propto \log(w_i f_X(x)) \tag{33a}$$

$$\log(n_i) \propto \log(w_i x^{\alpha}) \tag{33b}$$

If the bin width is some constant, $w_i = b$, then equation 33b results in

$$\log(n_i) \propto \log(b) + \alpha \log(x) \tag{34}$$

This regression would result in the correct value α. However as the PDF is an exponential function it may be several orders of magnitude larger for the smallest sample than the largest sample. This difference will directly carry over to the histogram with some bins containing several orders of magnitude more samples than others, and it is probable that some bins contain 0 samples. This reduces the accuracy of the regression and to avoid it logarithmic binning is used.

Logarithmic binning means that the logarithm of the lower edge of bin i and the logarithm of the lower edge of bin $i+1$ is separated by a distance b

$$\log(x_{i+1}) = log(x_i) + b \tag{35}$$

Exponentiating both sides results in

$$x_{i+1} = x_i e^b, \tag{36}$$

giving a bin width w_i

$$w_i = x_i \left(e^b - 1\right). \tag{37}$$

Inserting equation 37 into equation 33b and assuming $f_X(x) \propto x^{\alpha}$ results in

$$\log(n_i) \propto \log(x_i x_i^{\alpha}) \tag{38a}$$

$$\log(n_i) \propto (\alpha + 1)\log(x_i) \tag{38b}$$

This means that the exponent differs by one between logarithmic binning and constant binning.

B Geometric invasion models

B.1 Invasion percolation

Invasion percolation is a geometrical process that accurately models capillary fingering.

1. Each site on a $L_x \times L_y$ lattice is assigned a random threshold on the unit interval.
2. Each site on the bottom row is set to one, all other sites set to zero.
3. The zero-value-site adjacent to a one-value-site with the lowest threshold is set to one.
4. (Optional) If a region of zero-value-sites is completely surrounded by one-value-sites then these sites are assigned threshold 1, making invasion impossible.
5. Repeat step 3 and 4 until a site at the top row has been set to one.

B.2 Diffusion limited aggregation

Diffusion limited aggregation is a geometric process that accurately models viscous fingering. The algorithm is as follows:

1. A single site on the bottom row on a $L_x \times L_y$ lattice is set to one, all other sites are set to zero.

2. A random-walker is introduced at the top row. When the walker reaches a site adjacent to a one-value-site it stops and this site is set to one. The walker can only move to adjacent sites of its current position , it can never leave the lattice.

3. Repeat step 2 until a site at the top row is set to one.

B.3 Anti diffusion limited aggregation

Anti diffusion limited aggregation is a geometric process that accurately models stable displacement. The algorithm is as follows:

1. Set all sites on a $L_x \times L_y$ lattice to one.

2. Release a random walker at the bottom row. When the walker reaches a one-value-site it stops and the site is set to zero. The walker can only move to adjacent sites of its current position , it can never leave the lattice.

3. Repeat step 3 until a site at the top row is set to zero.

References

[1] Eyvind Aker, Knut Jørgen Måløy, Alex Hansen, and G.George Batrouni. A two-dimensional network simulator for two-phase flow in porous media. *Transport in Porous Media*, 32(2):163–186, 1998. ISSN 0169-3913. doi:10.1023/A:1006510106194. URL `http://dx.doi.org/10.1023/A%3A1006510106194`.

[2] Eyvind Aker, Knut Jørgen Måløy, and Alex Hansen. Simulating temporal evolution of pressure in two-phase flow in porous media. *Phys. Rev. E*, 58: 2217–2226, Aug 1998. doi:10.1103/PhysRevE.58.2217. URL `http://link.aps.org/doi/10.1103/PhysRevE.58.2217`.

[3] Eyvind Aker, Knut Jørgen Måløy, Alex Hansen, and Soumen Basak. Burst dynamics during drainage displacements in porous media: Simulations and experiments. *EPL (Europhysics Letters)*, 51(1):55, 2000.

[4] Jing-Den Chen and David Wilkinson. Pore-scale viscous fingering in porous media. *Physical review letters*, 55(18):1892–1895, 1985.

[5] Marek Cieplak and Mark O Robbins. Dynamical transition in quasistatic fluid invasion in porous media. *Physical review letters*, 60(20):2042–2045, 1988.

[6] Arthur K Doolittle. Studies in newtonian flow. i. the dependence of the viscosity of liquids on temperature. *Journal of Applied Physics*, 22(8):1031–1035, 1951.

[7] Marion Erpelding, Santanu Sinha, Ken Tore Tallakstad, Alex Hansen, and Knut Jørgen Måløy. History-independence of steady state in simultaneous two-phase flow through porous media. Submitted to Physical Review E. arXiv:1304.4753, 2013.

[8] Liv Furuberg, Knut Jørgen Måløy, and Jens Feder. Intermittent behavior in slow drainage. *Physical Review E*, 53(1):966, 1996.

[9] William B Haines. Studies in the physical properties of soil. v. the hysteresis effect in capillary properties, and the modes of moisture distribution associated therewith. *The Journal of Agricultural Science*, 20(01):97–116, 1930.

[10] Per C Hemmer and Alex Hansen. The distribution of simultaneous fiber failures in fiber bundles. *Journal of applied mechanics*, 59(4):909–914, 1992.

[11] S Irmay. On the theoretical derivation of darcy and forchheimer formulas. *Transactions, American Geophysical Union*, 39:702–707, 1958.

[12] R Lenormand, C Zarcone, and A Sarr. Mechanisms of the displacement of one fluid by another in a network of capillary ducts. *J. Fluid Mech*, 135(34): 337–353, 1983.

[13] Roland Lenormand and Cesar Zarcone. Invasion percolation in an etched network: measurement of a fractal dimension. *Physical review letters*, 54 (20):2226–2229, 1985.

[14] Roland Lenormand, Eric Touboul, and Cesar Zarcone. Numerical models and experiments on immiscible displacements in porous media. *Journal of Fluid Mechanics*, 189(9):165–187, 1988.

[15] Franziska Moebius and Dani Or. Interfacial jumps and pressure bursts during fluid displacement in interacting irregular capillaries. *Journal of colloid and interface science*, 2012.

[16] Knut Jørgen Måløy, Jens Feder, and Torstein Jøssang. Viscous fingering fractals in porous media. *Physical review letters*, 55(24):2688–2691, 1985.

[17] Knut Jørgen Måløy, Liv Furuberg, Jens Feder, and Torstein Jøssang. Dynamics of slow drainage in porous media. *Physical review letters*, 68(14): 2161–2164, 1992.

[18] Lincoln Paterson. Diffusion-limited aggregation and two-fluid displacements in porous media. *Physical review letters*, 52(18):1621–1624, 1984.

[19] JF Poco, JH Satcher Jr, and LW Hrubesh. Synthesis of high porosity, monolithic alumina aerogels. *Journal of non-crystalline solids*, 285(1):57–63, 2001.

[20] A. E. Scheidegger. *The physics of flow through porous media*. University of Toronto Press, third edition edition, 1974.

[21] Ken Tore Tallakstad. Steady-state, simultaneous two-phase flow in porous media. Master's thesis, University of Oslo, May 2007.

[22] Ken Tore Tallakstad, Grunde Løvoll, Henning Arendt Knudsen, Thomas Ramstad, Eirik Grude Flekkøy, and Knut Jørgen Måløy. Steady-state, simultaneous two-phase flow in porous media: An experimental study. *Physical Review E*, 80(3):036308, 2009.

[23] Edward W Washburn. The dynamics of capillary flow. *Physical review*, 17 (3):273, 1921.

[24] David Wilkinson and Jorge F Willemsen. Invasion percolation: a new form of percolation theory. *Journal of Physics A: Mathematical and General*, 16 (14):3365, 1983.

[25] TA Witten Jr and Leonard M Sander. Diffusion-limited aggregation, a kinetic critical phenomenon. *Physical Review Letters*, 47(19):1400–1403, 1981.